Magnetic field shimming of a permanent magnet using a combination of pieces of permanent magnets and a single-channel shim coil for skeletal age assessment of children

Y. Terada[*], S. Kono, K. Ishizawa, S. Inamura, T. Uchiumi, D. Tamada, and K. Kose

Institute of Applied Physics, University of Tsukuba, Tsukuba, Ibaraki 305-8573, Japan,

Abstract

We adopted a combination of pieces of permanent magnets and a single-channel (SC) shim coil to shim the magnetic field in a magnetic resonance imaging system dedicated for skeletal age assessment of children. The target magnet was a 0.3-T open and compact permanent magnet tailored to the hand imaging of young children. The homogeneity of the magnetic field was first improved by shimming using pieces of permanent magnets. The residual local inhomogeneity was then compensated for by shimming using the SC shim coil. The effectiveness of the shimming was measured by imaging the left hands of human subjects and evaluating the image quality. The magnetic resonance images for the child subject clearly visualized anatomical structures of all bones necessary for skeletal age assessment, demonstrating the usefulness of combined shimming.

Corresponding author: *terada@bk.tsukuba.ac.jp

I. INTRODUCTION

Skeletal age, which gives a measure of child growth, is evaluated by assessing the maturity of bones in the left hand and wrist [1-3]. Although plain radiography has been the gold standard for skeletal age assessment, magnetic resonance imaging (MRI) has recently emerged as an alternative [4-6] because of its noninvasive and nonirradiative nature. In a previous study [7], we showed the validity of skeletal age assessment using an open, compact MRI system. However, the magnetic circuit used in the previous work was designed to image an adult hand [8-10], and was large for young children (620 mm × 1006 mm × 620 mm in size, 700 kg in weight). Indeed, in some examinations, the arm of the subject was too short to reach the center of the imaging volume, and the unnatural posture of the body introduced a severe motion artifact that hampered the skeletal age rating. To remedy this problem, in this study, we used a smaller permanent magnet and developed a new, dedicated MRI system for the skeletal age assessment of children.

From a technical point of view, high homogeneity of the magnetic field in the imaging volume is required to obtain high-quality magnetic resonance (MR) images, because inhomogeneity leads to image artifacts such as signal loss and image distortion. The field homogeneity of a permanent magnetic circuit immediately after installation, however, is generally far from the imaging criteria, because of the manufacturing tolerance and variations and the influence of surrounding objects. Therefore, magnetic field shimming is required to compensate for the field inhomogeneity to meet the target imaging criteria.

The standard approach for passively shimming permanent magnets uses movable blocks or additional small pieces of permanent magnets. High homogeneity can be achieved by precisely positioning a number of shim pieces of permanent magnets. Different methodologies of passive shimming are being developed by a number of research and development groups, and there have been remarkable improvements in field homogeneity, especially in the fields of portable NMR/MRI with single-sided [11-16] and closed [17-22]

permanent magnets. The details including instrumentations and applications are reviewed elsewhere [23-26]. For example, the use of shim units built from movable permanent blocks and fine control of their positioning allow sub-ppm spectroscopic resolution sufficient to measure ^{1}H NMR spectra, in a single-sided magnet [13] and in a Halbach closed magnet [20]. In contrast, relatively few reports concerning passive shimming for open-type biplanar permanent magnets have been published. For such magnets, small pieces of magnetic material (iron/permanent magnets) are attached to a pole face for the fine-tuning of field homogeneity with the use of an iterative optimization algorithm [27-30].

The field homogeneity that can be obtained with passive shimming is limited by undesired errors in positioning shim magnet pieces. The higher homogeneity can be obtained by additional use of electrical shim coils [31], which further reduce residual field inhomogeneity beyond the limit of passive shimming. Furthermore, the homogeneity limit of passive and electrical shimming (or hardware shimming) can further be corrected by using sophisticated NMR measurement schemes such as nutation echoes [32] and shim pulse techniques [33-35].

Electrical current shims use multiple coils that are individually designed to correct a specific spherical harmonic distribution in field inhomogeneity. In some ideal cases, the spatial distribution of the magnetic field is stationary, and amplitudes of currents in shim coils are fixed. Then, multiple shim coils could be simplified to a single-channel (SC) shim coil that has a pattern designed by calculating the superposition of currents in the multiple shim coils that are determined to compensate for a given inhomogeneity. The concept of SC shimming has been used in the design of a biplanar shim coil for Halbach magnets [36-38].

SC shimming has the advantages of simplicity of hardware and installation space and could be an alternative to multichannel electrical shimming. Furthermore, the design and fabrication of SC shim coils are relatively simple and easy, whereas fine shimming with small

3

pieces of permanent magnets requires sophisticated techniques and much effort to maintain accuracy of positioning during the iterative process of shimming.

Like conventional electrical shimming, however, SC shimming has an upper limit of the correctable field strength and is not suitable for the compensation of large field inhomogeneities. This is because the current in an SC coil should be limited so as not to cause excess heat generation that degrades the field homogeneity. Therefore, it is practical and desirable to make use of SC shimming combined with coarse passive shimming with permanent magnet pieces.

In this study, the combined shimming was tested with experimental measurements of the magnetic field and evaluation of the quality of MR images. We first performed coarse shimming with pieces of small permanent magnets and then performed SC shimming to correct the residual high-order spatial inhomogeneity. In addition, we obtain MR images of the left hands of human subjects with the sequences used for MR skeletal examination in the previous study [7] and show that image artifacts are sufficiently suppressed so that anatomical structures of bones necessary for skeletal age assessment are clearly visualized in the MR images.

II. EXPERIMENTAL

A. Compact MRI system

Figures 1(a) and 1(b) are an overview and a photograph of the compact MRI system except for the MRI console. The spatial coordinates were defined as shown in the figure. The compact MRI system consisted of a C-type Nd-Fe-B permanent magnet (Shin-Etsu, Chemical Co. Ltd, Tokyo, Japan), a gradient coil set, an RF probe, and an MRI console. The specifications of the permanent magnet were: a field strength of 0.3 T, gap width of 120 mm, dimensions of 400 mm × 570 mm × 410 mm, and weight of 450 kg. This magnetic circuit was roughly shimmed using Nd-Fe-B magnet plates by the manufacturer, and the magnetic

field homogeneity was not high (350 ppm (root mean square, RMS) and 1500 ppm (peak-to-peak, PP) over 160 mm × 160 mm × 50 mm diameter ellipsoidal volume (DEV)). The magnet was kept at 28 °C because the magnetic field strength and spatial variation were sensitive to temperature changes [38].

We used a solenoid RF coil optimized for imaging a child's hand that was the same as the coil used in the previous work [7]. The coil was a 16-turn solenoid, 17.6 cm long, and was made by winding Cu foil (0.1 mm thick) around an oval acrylic pipe (aperture: 10 cm × 5 cm; length of 220 mm; thickness of 4 mm) and divided in quarters with three chip capacitors (100 pF) to reduce stray capacitance between the hand and coil. The RF coil was shielded by a rectangular RF probe box made of 0.3-mm-thick brass plates. A 5-mm-thick aluminum plate was connected to the outside of the brass box to ground the arm and thus minimize interference by external RF noise [8]. The typical duration of the 90° hard pulse was 120 μs using an output power of 200 W.

B. Gradient coil design

The x- and y-gradient coils were designed as a combination of a circular arc and third-order Bezier curve with the position and center angle optimized using a genetic algorithm with a minimal generation gap model (GA/MGG) [39,40]. The maximum number of turns was 30 and the coil gap was set to 120 mm. The z-gradient coil was designed as a combination of circular current loops with diameter optimized using a GA/MGG. The maximum number of turns was 40 and the coil gap was set to 105 mm. In each calculation, the wire diameter was set to 1 mm and the coil pattern was restricted to a circular region with a diameter of 320 mm. The number of iterations was 100,000 and the total calculation time was almost a week for the x- and y-gradient coils and three days for the z-gradient coil using a 2.7-GHz clock-frequency Pentium dual-core processor. The calculated nonlinearity of the

gradient field of the x-, y-, and z-gradient coils was 9.1%, 9.1%, and 7.6% in 180 mm × 180 mm × 60 mm DEV, respectively.

Each gradient coil element was made by winding polyethylene-coated Cu wire (1 mm in diameter) on the surface of a fiber-reinforced plastic (FRP) plate (360 mm in diameter, 0.5 mm thick) and tracing a printed coil pattern attached on the other side of the plate (Fig. 1(c)); x, y, and z coil elements were then stacked together using epoxy resin. The gradient coil elements were driven by a three-channel gradient driver (±10 A, DGD10AT, Digital Signal Technology, Inc., Saitama, Japan). The measured efficiency of the x-, y-, and z-gradient coils was 2.28, 2.32, and 3.11 mT/m/A, the resistance was 1.4, 1.4, and 1.2 Ω, and the inductance was 390, 260, and 250 μH, respectively.

C. Target region of interest for shimming

The typical size necessary for the MR skeletal examination of children aged 12 years is 80 mm (x) × 155 mm (y) × 25 mm (z). Accordingly, we determined the target region of interest (ROI) for shimming to be a 120 mm × 160 mm × 50 mm DEV.

D. Evaluation of the magnetic field inhomogeneity

The spatial variation in the magnetic field B_0 was measured using two methods according to the order of the homogeneity. When the B_0 homogeneity was low at the initial stages of shimming, the variation was measured by a nuclear magnetic resonance (NMR) probe. The probe consisted of a solenoid RF coil wound around a 6-mm diameter glass sphere filled with baby oil (Johnson & Johnson, Skillman, NJ, USA), tuning and matching capacitors, and a rectangular shield box made of brass plates (50 mm × 60 mm × 25 mm). To measure the B_0 inhomogeneity, the NMR probe was positioned in the magnet gap by a three-axis stage with accuracy of 0.1 mm, and the free induction decay (FID) signal was measured at the given position. The magnetic field was then determined by the peak center of

the Fourier transform of the FID signal. Likewise, the magnetic fields at grid points 1 cm apart in a rectangular area (160 mm × 160 mm) were measured.

When the homogeneity was improved to a high level, the B_0 spatial variation was evaluated employing a conventional MRI-based, phase-shift method with a phantom made of a cylindrical acrylic container (200 mm in diameter, 55 mm high) filled with $CuSO_4$-doped water. This method is more accurate and efficient than the above NMR probe-based method.

The measured B_0 spatial variations were expanded as follows:

$$\Delta B_0(r) = A_{00} + \sum_{l,m}(A_{lm+}C_{lm} + A_{lm-}S_{lm} + A_{l0}J_{l0}),$$ where the coefficients A_{lm+}, A_{lm-}, and A_{l0}

make reference to the combinations of the spherical harmonics $C_{lm} \equiv (-1)^m r^l \frac{1}{\sqrt{2}}(Y_{lm} + Y_{lm}^*)$,

$S_{lm} \equiv (-1)^m r^l \frac{1}{\sqrt{2}}(Y_{lm} - Y_{lm}^*)$, and $J_{l0} \equiv r^l Y_{l0}$. Here $Y_{lm} \equiv (-1)^l \left(\frac{2l+1}{4\pi}\right)^{1/2} P_l^m(\cos\theta)e^{im\phi}$,

where P_l^m represents the Legendre polynomials.

E. Passive shimming using small pieces of permanent magnets

We initially performed manual passive shimming to correct the inhomogeneity produced by manufacturing errors of the magnet. The sizes of rectangular Nd-Fe-B permanent magnet pieces used for shimming were (18 mm)^2 × 1 mm, (13 mm)^2 × 1 mm, (5.6 mm)^2 × 1 mm, (3.6 mm)^2 × 1 mm, (3 mm)^2 × 1 mm, and (1 mm)^3. Prior to the passive shimming, the B_0 spatial distribution generated by a permanent shim magnet piece was measured for several different magnet sizes. The position and number of compensating shim magnets were then determined by a method similar to that described in Ref. 29. First, the B_0 distribution was measured, and the values of B_0 at points located near the boundary of the target ROI were compared with each other. Among those, point i, where the magnetic field was at maximum or minimum, was chosen. If B_0 at point I was lower (higher) than at the center of the ROI, a positive (negative) shim magnet was set on the point projected on the

closest pole surface. Here, if the point *i* was in the upper (lower) hemispherical region, the upper (lower) pole surface was chosen. The size of the shim magnet was determined in such a way that the calculated RMS ΔB_0 was minimized. The number of magnets placed at one shim stage was typically 10 and this step was repeated until the shim magnet was a 1-mm cube and the RMS ΔB_0 was almost unchanged. Although this manual shimming was time-consuming and inefficient, it enabled us to compensate for the large, low-order spatial inhomogeneity as will be shown later. More efficient methods for biplanar passive shimming have been realized with an optimization algorithm used to cancel a set of field harmonics and to minimize the volume of an array of shim pieces [27,28].

F. Shimming using an SC shim coil

After the passive shimming, a shim coil set was designed to correct the residual inhomogeneity. The design method was based on the superposition of multiple circular currents (MCCs) [41,42], which is similar to the method reported previously [37]. In the previous work, the magnet gap where the SC coil was placed was narrow, and the stream function (SF) method [43] was used after the MCC calculation to obtain the flat coil pattern and reduce the coil space. In the present method, the space for the SC coil was sufficient and the SF method was not used to avoid a potential error field arising from the SF method and to simplify the calculation.

In the MCC method, the magnetic field B_s generated by the SC shim coil is a linear combination of the magnetic field B_{ij} generated by circular unitary currents placed on an $n \times m$ elliptical grid: $B_s = \sum_{i=1}^{n} \sum_{j=1}^{m} c_{ij} B_{ij}$, where c_{ij} is the coefficient for the linear combination. The coefficients were determined using a nonlinear least-squares method to fit B_s to compensate for the B_0 variation. During the iteration process, the maximum and minimum of the coefficients were restricted to +15 and −15, respectively, to suppress the net current and

avoid excess heating of the coil. The coefficient c_{ij} was then rounded off to the nearest integer, by which the number of turns of the coil at the (i, j) position was determined.

As shown in Fig. 1(d), an SC shim coil element was made by winding a polyethylene-coated Cu wire (0.4 mm in diameter) around acrylic pipes (20 mm in outer diameter, 4 mm in height) fixed on an elliptical 7×9 grid with 22-mm intervals. The coil was then fixed on an FRP plate (360 mm $\times$ 360 mm, 0.5 mm thick) using epoxy resin. The resistance of the SC shim coil was 8.2 Ω.

G. Demonstration of the system performance

The left hand of a healthy female volunteer aged 22 years was imaged to evaluate the image quality after SC shimming. Furthermore, the left hand of a healthy female volunteer aged 4.9 years was imaged to test the ability of the system to assess the skeletal age. Written informed consent was obtained from both the child and one of the parents. All MRI measurements were performed with the approval of the Ethics Committee of the Graduate School of Pure and Applied Sciences, University of Tsukuba.

The sequence parameters were the same as those used in the previous work [7]. A three-dimensional (3D) coherent gradient-echo (GE) sequence was used (dwell time of 20 μs; repetition time (TR)/echo time (TE) of 40/11 ms; flip angle of 60°; matrix size of $512 \times 128 \times 32$; field of view (FOV) of 200 mm $\times$ 100 mm $\times$ 50 mm; and total acquisition time of 2 min 44 s).

Using the MR images, the skeletal age for the 4.9-year-old volunteer was rated according to the Tanner–Whitehouse (TW2) Japan RUS system (where RUS stands for the radius, ulna, and 11 short bones in rays 1, 3, and 5) [44].

III. RESULTS

A. Passive shimming using small pieces of permanent magnets

Figure 2 shows an improvement in B_0 homogeneity (measured using the NMR probe method) during the passive shimming with permanent magnet pieces. As the shimming proceeded, B_0 became homogenous (Fig. 2(a)). The passive shimming was repeated until the RMS ΔB_0 was almost constant. With the passive shimming, the RMS ΔB_0 decreased from 347 to 19.6 ppm and the PP ΔB_0 decreased from 1180 to 266 ppm (TABLE I). Figures 2(b) and 2(c) are histograms of ΔB_0 at the initial and final stages of the passive shimming, showing a drastic improvement in homogeneity. Figures 2(d) and 2(e) show the B_0 spatial variations before and after passive shimming. Figure 3 shows the contribution of the different orders to the field variations in the target ROI before and after the passive shimming. Figure 4(a) shows the B_0 spatial variation and its histogram after the passive shimming, as measured using the phase-shift method. The figure shows that there still existed local inhomogeneity even after the passive shimming.

B. SC shimming

According to the above result, the SC shim coil was designed and fabricated (Fig. 1(d)) to correct the residual inhomogeneity. Figure 4(b) shows the B_0 variation and its histogram with SC shimming. It is seen that the residual inhomogeneity was largely compensated for by the SC shimming. The inhomogeneity decreased to 14.3 ppm (RMS) and to 160 ppm (PP) (TABLE I). Figure 5 shows the contribution of the different orders to the field variations in the target ROI before and after the SC shimming.

C. Demonstration of system performance

Figure 6 shows coronal sections of 3D GE images of the left hand of a healthy 22-year-old volunteer acquired at different stages of shimming. At the initial stage before magnet and SC shimming (Fig. 6(a)), a large part of the hand could not be imaged because of the large signal loss due to B_0 inhomogeneity. In contrast, after passive shimming (Fig. 6(b))

most of the bones were clearly visualized. However, there still existed local, critical signal loss in the images (circled in white), and hence the detailed skeletal features of the ulna and radius, which are highly important in the RUS skeletal rating, were not visualized. Meanwhile, after SC shimming (Fig. 6(c)), the local inhomogeneity improved and both the ulna and radius bones were clearly visualized.

Figure 7 shows coronal sections of the 3D GE images for a healthy 4.9-year-old volunteer acquired after magnet and SC shimming. The morphological features of the epiphyses and diaphyses of RUS bones, which are needed for the TW2 skeletal rating, could be discriminated in the images. For example, the epiphysis and diaphysis of the distal phalanx in ray 3 were visible in slice number 20 (magnified image in Fig. 7), and the length of the epiphysis was more than half but less than the length of the diaphysis. This maturity indicator assigns the bone to developmental stage E according to the TW2 Japan RUS system. Likewise, by judging the developmental stages of other bones, the skeletal age of the subject was determined to be 5.0 years old, which was close to her chronological age (4.9 years old), thus revealing the validity of the result.

IV. DISCUSSION

First, we discuss the differences in the RMS and PP values measured using the NMR probe and phase-shift methods (TABLE 1). In the NMR probe method, the diameter of the NMR probe was 6 mm and the spatial resolution was poor. Moreover, the magnetic field within the volume of the NMR probe was significantly inhomogeneous at the initial shimming stage or near the edge of the target ROI. In this case, the NMR signal rapidly decayed and broad spectra were obtained, leading to large errors in the determination of the peak position in the NMR spectra. Therefore, the NMR probe method gave only a rough estimate of the magnetic field. In contrast, the phase-shift method gave a more accurate estimate at the pixel spatial resolution.

Next, we focus on the effectiveness of the combined shimming. Before the passive and SC shimming, the magnetic field was inhomogeneous and the left hand of the subject could hardly be visualized in the GE images because of the large signal loss. After passive shimming, the field homogeneity was drastically improved and the RMS ΔB_0 decreased by 94% (TABLE I). Although a large part of the hand could be visualized, there was still local inhomogeneity. The subsequent SC shimming enabled the compensation of the local inhomogeneity that could not be compensated for by the passive shimming. This improvement led to the recovery of the signal loss around the ulna and radius bones.

Figures 3 and 5 show the field profiles before and during different stages of shimming. The passive shimming largely compensated for almost all field-skewed terms up to the 6th order (Fig. 3). However, the large skewed terms of orders 4 and 6 remain even at the final stage of passive shimming. Near the final stage, the size of shim magnets was 1 mm, and their precise positioning became increasingly difficult and time-consuming. Although the higher homogeneity could be achieved by using fine mechanics for positioning shim magnets more accurately, it is practically difficult to achieve it at a reasonable cost. In contrast, most of the residual skewed terms of orders 4 and 6, as well as the lower-order terms were further corrected by SC shimming (Fig. 5). These higher terms cannot be corrected by conventional, lower-order shim coils and these results demonstrate the effectiveness of the combined passive and SC shimming.

The use of SC shimming was superior to conventional electrical shimming in terms of simplicity of the hardware and space required, but it imposed a limitation on the maximum current used. TABLE II summarizes the theoretical performance of the SC and conventional shim coils. Here the latter coils were designed using rectangular current loops proposed by Anderson [31]. The installation space for the SC shim coil was much narrower than the conventional coil, and the theoretical value of RMS ΔB_0 was also smaller. However, much higher power is required for the SC shim coil. The resulting heat is likely to cause a

temperature increase of the magnetic circuit, leading to deterioration in the field homogeneity. This is often the case where an SC shim coil is located near pole pieces that are sensitive to temperature drift. The deterioration in homogeneity can be overcome by reducing power dissipation with the combined use of the MCC method, SF method, and power optimization algorithm. Recently we experimentally showed that with a power-optimized SC shim coil, there is negligible heat generation and negligible degradation of the magnetic field in continuous use [45].

As shown in TABLE II, the theoretical RMS value was 6.0 ppm with SC shimming, which differed from the measured value. The difference may be attributed to fabrication errors in the circular coils. Because of the finite width of the coil, the position of each circular coil differs from the ideal position, in particular in the gap direction. Calculation considering the coil width would lead to a better compensation of B_0 inhomogeneity.

Another issue is that, in contrast to conventional electrical shimming, SC shimming compensates for only a defined ("fixed") spatial dependence of inhomogeneity. The spatial distribution of the magnetic field depends on different conditions such as the temperature of the system, the proximity of the C-type magnet to ferromagnetic objects (walls and doors), or even in some cases on sample susceptibilities effects. The effect of the temperature change of the system may be avoidable; it has been revealed that for a Halbach-type closed magnet, the inhomogeneity has a specific spatial symmetry, which scales linearly with temperature, and that the inhomogeneity was drastically reduced by SC shimming over a wide temperature range [38]. The influence of ferromagnetic objects is also avoidable by taking care not to place them near the system. The effects of sample susceptibilities are mostly negligible for low-field MRI systems as in the present case (unlike the case for high-field systems).

There is still magnetic field inhomogeneity even after SC shimming. The residual inhomogeneity may lead to two classes of image artifacts in GE images. The first artifact is image distortion along the read (y) direction. This is caused by the local background gradient

field $G_y^{'}$ due to the local field variation along the read direction, where $G_y^{'}$ is calculated

from the measured ΔB_0 as $G_y^{'} = \dfrac{\partial \Delta B_0}{\partial y}$. With the presence of $G_y^{'}$, the local effective FOV

in the read direction is scaled [19,20] by the factor $\lambda = \dfrac{G_y}{G_y + G_y^{'}}$,where

$G_y = \left(\dfrac{\gamma}{2\pi} \cdot \Delta t \cdot N_y \right)^{-1}$ is the gradient field in the read direction, γ ($= 2\pi \times 42.58$ MHz) is

the gyromagnetic ratio of the proton, Δt is the dwell time, and N_y is the number of

sampling points in the read direction. There is large distortion where the value of λ is far

from unity. The histograms of λ derived from the present parameters ($\Delta t = 20$ µs and N_y

= 512) and the measured ΔB_0 after SC shimming show that most of the values of λ are

close to unity, indicating that the local distortion is sufficiently small (Fig. 8(a)).

The second artifact arising from the inhomogeneity is signal loss due to intravoxel

dephasing. The local background gradients along the x, y, and z directions ($G_x^{'}$, $G_y^{'}$, and

$G_z^{'}$) cause the shift of the echo center in the k_x, k_y, and k_z directions, respectively. In the

read direction, in the limit of $\left| G_y^{'} \right| << G_y$, the echo shift, $\delta_y N_y$, measured in units of the

sampling points, is approximated by [46,47] $\delta_y N_y \approx \gamma G_y^{'} \cdot TE \cdot L_y$, where TE is the echo

time, and N_y and L_y are the number of sampling points and the FOV size in the read

direction, respectively. There is large signal loss when the echo is completely shifted outside

the acquisition window ($\left| \delta_y \right| = 0.5$). This gives an upper limit for the tolerable signal loss

under given imaging conditions ($TE = 11$ ms and $L_y / N_y = 0.39$ mm in the present case).

In the histogram of δ_y derived from the calculated $G_y^{'}$, the ratio of area where $\left| \delta_y \right| > 0.5$

is only 0.09 % of the total ROI, indicating that the corresponding signal loss is sufficiently small (Fig. 8(b)).

In the two phase-encoding directions, the echo shifts in the k-space, $\delta_x N_x$ and $\delta_z N_z$, measured in units of sampling points, are given by $\delta_x N_x = \gamma G_x' \cdot TE \cdot L_x$, $\delta_z N_z = \gamma G_z' \cdot TE \cdot L_z$, where L_x and L_z are the FOV sizes along the x and z directions, respectively. As in the read direction, the rule of thumb to avoid total signal loss is that $|\delta_x| < 0.5$ and $|\delta_z| < 0.5$. Since $G_x' \approx G_z'$ and $L_x/N_x < L_z/N_z$ in the present case, the echo shift in the z direction is the most prominent cause for the signal loss. In the histogram of δ_z calculated from ΔB_0 measured after SC shimming, the ratio of area where $|\delta_z| > 0.5$, which corresponds to the signal-loss area, is 9.5% of the total ROI (Fig. 8(c)). This ratio was originally 14.2% before SC shimming, revealing that SC shimming largely suppressed the signal loss.

In general, the signal-loss area could further be reduced by selecting a shorter TE and smaller voxel sizes as imaging parameters. In the present case, however, TE must be fixed so that high contrast-to-noise ratio between the bone and surrounding cartilage is obtained because of the effect of fat–water frequency separation. In contrast, the voxel size in the z direction could be decreased and, for example, doubled N_z with fixed L_z would result in a decrease in the signal-loss area to only 1.6% of the total ROI.

The major advantage of the present system is that a small magnetic circuit is used. Its size is about 66% of that of the magnetic circuit used in the previous work [7], which enhances the openness and compactness of the system. The distance from the edge of the magnetic circuit to the center was 20 cm. This was short enough for the 4.9-year-old volunteer, for whom the length from the end of the finger to the shoulder joint was approximately 40 cm. It was thus easy to position the volunteer comfortably during the MR

examination (Fig. 1(b)). The use of a smaller magnet enhances openness and compactness, and the new system would provide stress-free and less fearful examinations for children over a wide range of ages.

The target ROI for shimming was set to 12 cm × 16 cm × 5 cm DEV, which is sufficiently large for the hands of children aged 12 or under. For children aged around 12 or over, the whole hand and wrist may not be visualized at a time. However, these older children might be tolerant of a longer measurement time, and the wrist and distal hand could thus be imaged separately.

V. CONCLUSION

We developed a dedicated, open and compact MRI system for assessment of children's skeletal age using a small magnetic circuit. The magnetic field was inhomogeneous at first and was drastically improved by combined magnet and SC shimming. SC shimming in particular allowed us to compensate for local inhomogeneity that could not be corrected by passive shimming. The performance of the present MRI system was evaluated in the hand imaging of two subjects. The quality of MR images was high enough for skeletal age assessment and the results demonstrate the usefulness of the combined shimming.

REFERENCES

[1] W. W. Greulich and S. I. Pyle, Radiographic atlas of skeletal development of the hand and wrist. 2nd ed., Stanford University Press, California, 1959.

[2] J. M. Tanner, Assessment of skeletal maturity and prediction of adult height (TW2 method). 2nd ed., Academic Press, London, New York, 1983.

[3] R. M. Acheson, J. Anat. 88 (1954) 498.

[4] J. Dvorak, J. George, A. Junge, and J. Hodler, Br. J. Sports Med. 41 (2007) 45.

[5] J. George, J. Nagendran, and K. Azmi, Br. J. Sports Med. 2010. doi:10.1136/bjsm.2010.074948.

[6] J. Dvorak, J. George, A. Junge, and J. Hodler, Br. J. Sports Med. 41 (2007) 497.

[7] Y. Terada, S. Kono, D. Tamada, T. Uchiumi, K. Kose, R. Miyagi, E. Yamabe, H. Yoshioka, Proc. Intl. Soc. Mag. Reson. Med. 20, (2011) 1448; Y. Terada, S. Kono, D. Tamada, T. Uchiumi, K. Kose, R. Miyagi, E. Yamabe, and H. Yoshioka, Skeletal age assessment in children using an open compact MRI system, accepted in Magnetic Resonance in Medicine. doi: 10.1002/mrm.24439.

[8] S. Handa, T. Haishi, and K. Kose, Rev. Sci. Instrum. 79 (2008) 113706.

[9] H. Yoshioka, S. Ito, S. Handa, S. Tomiha, K. Kose, T. Haishi, A. Tsutsumi, and T. Sumida, J. Magn. Reson. Imaging. 23 (2006) 370.

[10] T. Suzuki, S. Ito, S. Handa, K. Kose, Y. Okamoto, M. Minami, M. Sugihara, M. Horikoshi, H. Tsuboi, T. Hayashi, D. Goto, I. Matsumoto, and T. Sumida, Mod. Rheumatol. 20 (2010) 331.

[11] J. Perlo, V. Demas, F. Casanova, C.A. Meriles, J. Reimer, A. Pines, Science 308 (2005) 1279.

[12] J. Perlo, F. Casanova, and B. Blümich, J. Magn. Reson. 180 (2006) 274.

[13] J. Perlo, F. Casanova, and B. Blümich, Science 315 (2007) 1110.

[14] A. E. Marble, I. V. Mastikhin, B. G. Golpitts, and B. J. Balcom, J. Magn. Reson. 186 (2007) 100.

[15] J. L. Paulsen, L. S. Bouchard, D. Graziani, B. Blümich, and A. Pines, PNAS 105 (2008) 20601.

[16] M. V. Landeghem, E. Danieli, J. Perlo, B. Blümich, and F. Casanova, J. Magn. Reson. 215 (2012) 74.

[17] H. Raich and P. Blümler, Concepts Magn. Reson. 23B (2004) 16.

[18] R. C. Jachmann, D. R. Trease, L. -S. Bouchard, D. Sakellariou, R. W. Martin, R. D. Schlueter, T. F. Budinger, and A. Pines, Rev. Sci. Instrum. 78 (2007) 035115.

[19] A. McDowell and E. Fukushima, Appl. Magn. Reson. 35 (2008) 185.

[20] E. Danieli, J. Mauler, J. Perlo, B. Blümich, and F. Casanova, J. Magn. Reson. 198 (2009) 80.

[21] E. Danieli, J. Perlo, B. Blümich, and F. Casanova, Angew. Chem. Int. Ed. 49 (2010) 4133.

[22] C. Hugon, F. D'Amico, G. Aubert, and D. Sakellariou, J. Magn. Reson. 205 (2010) 75.

[23] B. Blümich, J. Perlo, and F. Casanova, Progr. Nucl. Magn. Reson. Spectr. 52 (2008) 197.

[24] V. Demas and P. Prado, Concepts in Magn. Reson. 34A (2009) 48.

[25] B. Blümich, F. Casanova, and S. Appelt, Chem. Phys. Lett. 477 (2009) 231.

[26] B. Blümich, F. Casanova, M. Dabrowski, E. Danieli, L. Evertz, A. Haber, M. V. Landeghem, S. H. Pohlmeier, A. Olaru, J. Perlo, and O. Sucre, New J. Phys. 13 (2011) 015003.

[27] T. Matsuda, A. Ariyoshi, and H. Tanabe, IEEJ Trans. Ind. Applicat., 125 (2005) 774.

[28] H. S. Lopez, F. Liu, E. Weber , and S. Crozier, IEEE Trans. Magn., 44 (2005) 394.

[29] Z. Ren, D. Xie, and H. Li, Progress in Electromagnetic Research M, 6 (2009) 23.

[30] L. Hong and D. Zu, PIERS Online, 3 (2007) 859.

[31] W. A. Anderson, Rev. Sci. Instrum. 32 (1961) 241.

[32] C. A. Meriles, D. Sakellariou, H. Heise, A. J. Moulé, and A. Pines, Science 293 (2001) 82.

[33] D. Topgaard, R. Martin, D. Sakellariou, C. A. Meriles, and A. Pines, Proc. Natl. Acad. Sci. U.S.A. 101 (2004) 17576.

[34] B. Shapira and L. Frydman , J. Am. Chem. Soc. 126 (2004) 7184.

[35] J. M. Franck, V. Demas, R. W. Martin, L-S. Bouchard, and A. Pines, J. Chem. Phys. 131

(2009) 234506.

[36] D. Tamada, Y. Terada, and K. Kose, Appl. Phys. Express 4 (2011) 066702.

[37] D. Tamada, K. Kose, and T. Haishi, Appl. Phys. Express 5 (2012) 056701.

[38] Y. Terada, D. Tamada, and K. Kose, J. Magn. Resonance 212 (2011) 355.

[39] H. Satoh, M. Yamamura, and S. Kobayashi, Minimal generation gap model for Gas considering both exploration and exploitation. In Proceedings of the 4th International Conference on Soft Computing, Iizuka, Japan, 30 September-5 October 1996, pp 494-497.

[40] D.-X. Gong, X.-G. Ruan, and J.-F. Qiao, Neural Comput. Applic. 13 (2004) 221.

[41] C. Juchem, T. W. Nixon, S. McIntyre, D. L. Rothman, and R. A. de Graaf, J. Magn. Reson. 204 (2010) 281.

[42] C. Juchem , T. W. Nixon, S. McIntyre, V. O. Boer, D. L. Rothman, and R. A. de Graaf, J. Magn. Reson. 212 (2011) 280.

[43] R. Turner, Magn. Reson. Imaging 11 (1993) 903.[44] Japanese Society for Pediatric Endocrinology & The Japanese Association for Human Auxology eds. Medical View, Tokyo, Japan (2011) (in Japanese).

[45] Y. Terada, K. Ishi, D. Tamda, and K. Kose, Appl. Phys. Express 6 (2013) 026701.

[46] J. R. Reichenbach, R. Venkatesan, D. A. Yablonskiy, M. R. Thompson, S. Lai, and E. M. Haacke, J. Magn. Reson. Imag. 7 (1997) 266.

[47] E. M. Haacke, R. W. Brown, M. R. Thompson, and R. Venkatesan, *Magnetic Resonance Imaging: Physcial Principles and Sequence Design* (Wiley-Liss, New York, 1999), p.570-588.

Figure captions

Fig. 1 (a) Schematic diagram of the open and compact MRI system dedicated to skeletal age examination, except the MRI console. (b) Overview of the skeletal age examination of a 4.9-year-old volunteer. (c) Coils for the z-gradient (G_z) and for the x- and y-gradients (G_x and G_y). (d) SC shim coil.

Fig. 2 Inhomogeneity compensation by passive shimming using the small pieces of permanent magnets. (a) RMS and PP ΔB_0, measured using the NMR probe method, as a function of the number of passive shimming steps. (b), (c) B_0 histograms (b) at the initial stage and (c) when passive shimming was complete. (d), (e) Spatial maps of ΔB_0 (d) at the initial stage and (e) when passive shimming was complete. Note that the color scales differ by one order of magnitude.

Fig. 3 Contributions of the different orders to the field variation in the target ROI at initial and final stages of passive shimming.

Fig. 4 Spatial maps and histograms of ΔB_0, measured using the phase-shift method, (a) after passive shimming (without SC shimming) and (b) after SC shimming.

Fig. 5 Contributions of the different orders to the field variation in the target ROI without and with SC shimming.

Fig. 6 MR images for the left hand of a 22-year-old volunteer acquired (a) at the initial stage of shimming, (b) after passive shimming (without SC shimming), and (c) with SC shimming. The figure in each image is the slice number. The FOV was 200 mm × 100 mm × 50 mm.

Fig. 7 MR images for the left hand of a 4.9-year-old volunteer acquired after all shimming was complete. The figure in each image is the slice number. The FOV, which was originally 200 mm × 100 mm × 50 mm, was trimmed (150 mm × 100 mm × 50 mm) for clarification. The epiphysis and diaphysis of the distal phalanx in ray 3 are magnified in the image of slice number 20.

Fig. 8 Estimation of image artifacts that may appear in GE images. (a) Histogram of the scaling factor λ of the local effective FOV in the read direction, calculated from ΔB_0 with the SC shimming measured using the phase-shift method. (b) Histogram of the calculated echo shift δ_y in the y (read) direction. (c) Histogram of the calculated echo shift δ_z in the z direction.

TABLE I. RMS and PP values of the magnetic field at different shim stages.

Shim stage	RMS (ppm)	PP (ppm)
Initial	347[*1]	1180[*1]
After shimming using small	19.6[*1]	266[*1]
magnet pieces	21.7[*2]	212[*2]
Final (after SC shimming)	14.3[*2]	160[*2]

[*1] Measured with the NMR probe. [*2] Measured using the phase-shift method.

TABLE II. Theoretical performances of the SC shim coil and conventional multichannel shim coils. The multichannel coils consisted of rectangular, 1st- and 2nd-order Anderson-type coils with a diameter of 0.4 mm. The thickness of the plate supporting the coil was assumed to be 0.5 mm.

	SC shim coil	Anderson-type shim coils
RMS ΔB_0	6.0 ppm (14.3 ppm[*1])	16.8 ppm
Installation space	0.9 mm	7.2 mm
Power	7.3 W	0.89 W

[*1] Measured value using the phase-shift method.

(a) 400mm 570mm

410mm

Gradient+
SC shim coils

Main magnet Shim magnet pieces Pole piece RF probe

(b) z x y

(c) 320mm

Gz Gx, Gy

Gradient coils

(d) 220mm 176mm

y x

SC shim coil
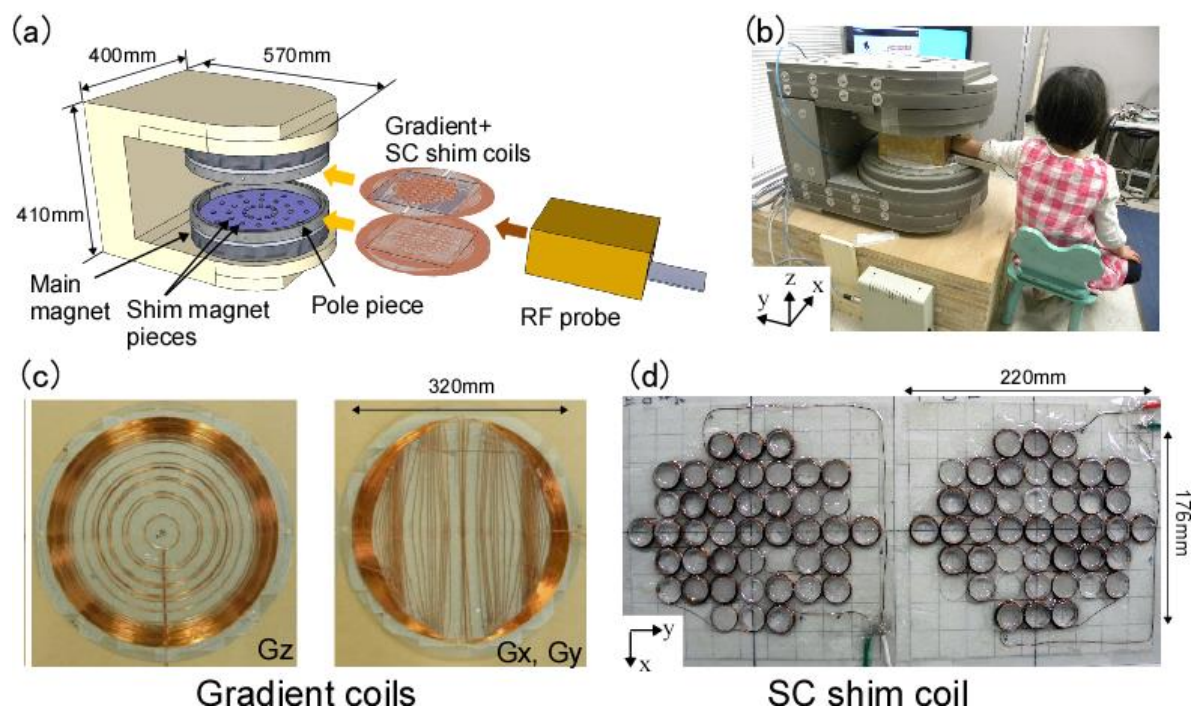
Fig. 1
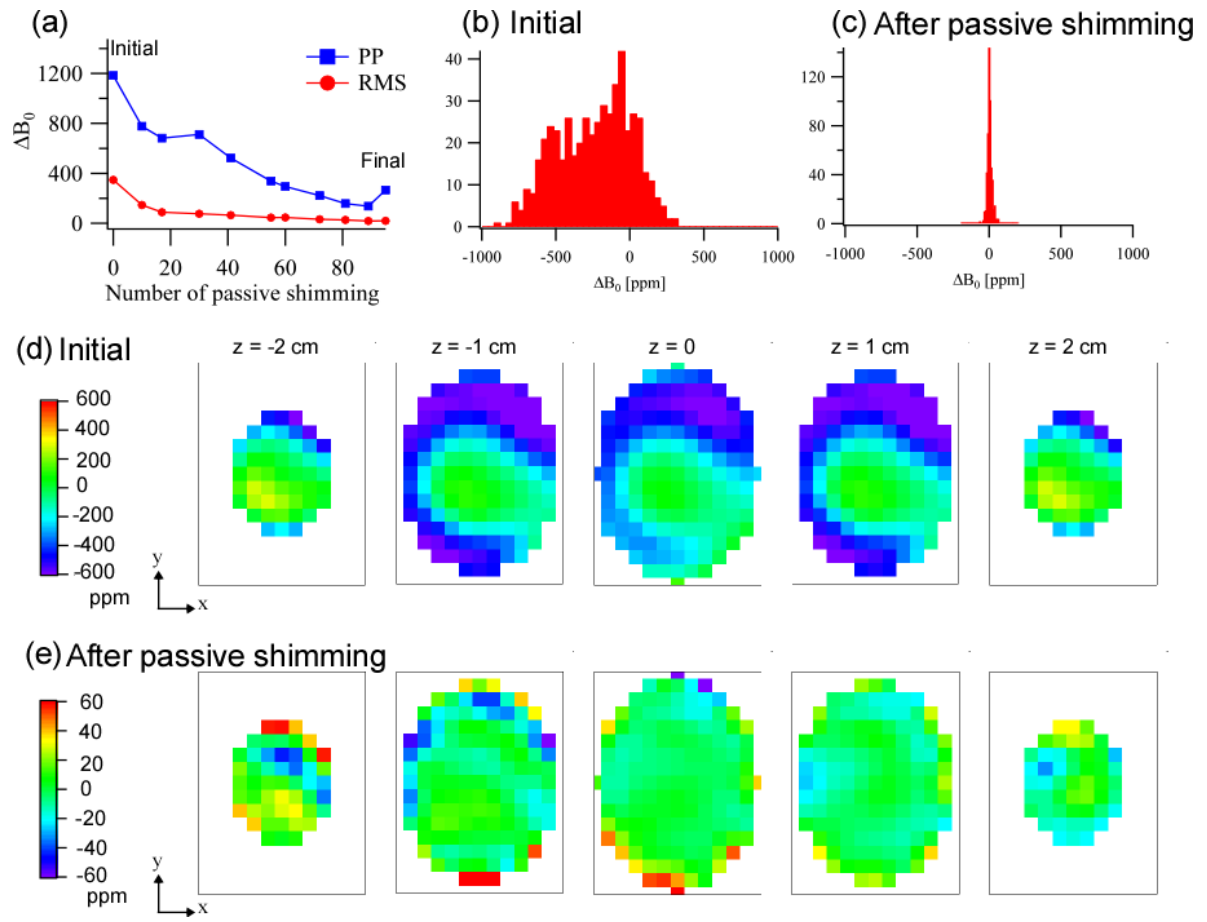
Fig. 2

Fig. 3

(a) After passive shimming

z = -2 cm   z = -1 cm   z = 0   z = 1 cm   z = 2 cm

(b) With SC shimming

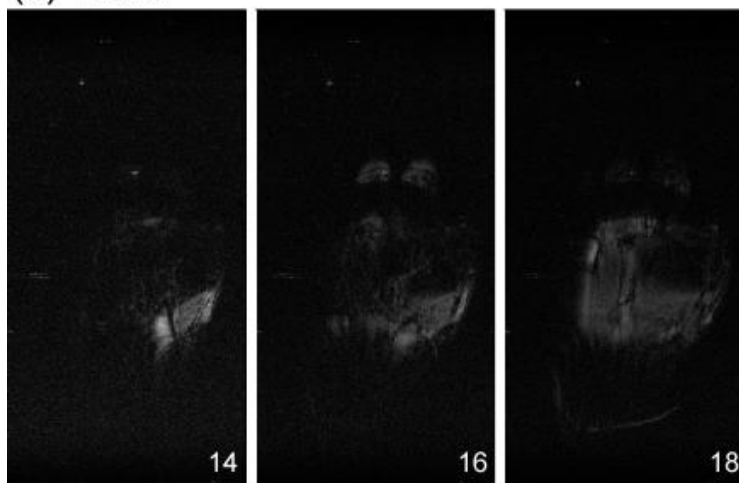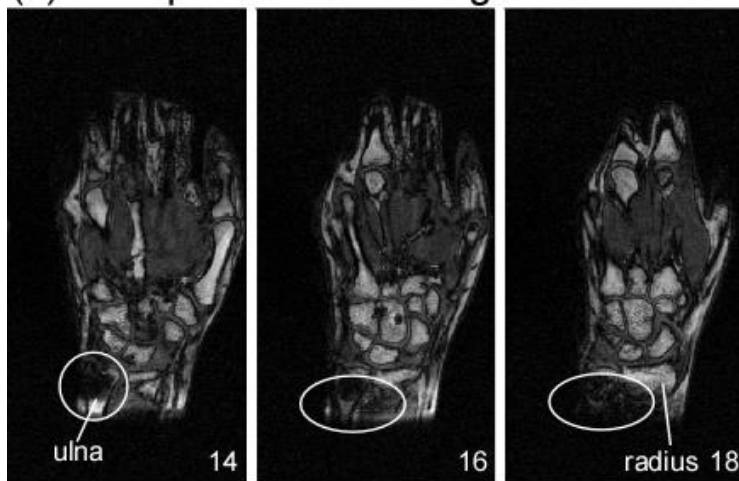z = -2 cm   z = -1 cm   z = 0   z = 1 cm   z = 2 cm

Fig. 4

29
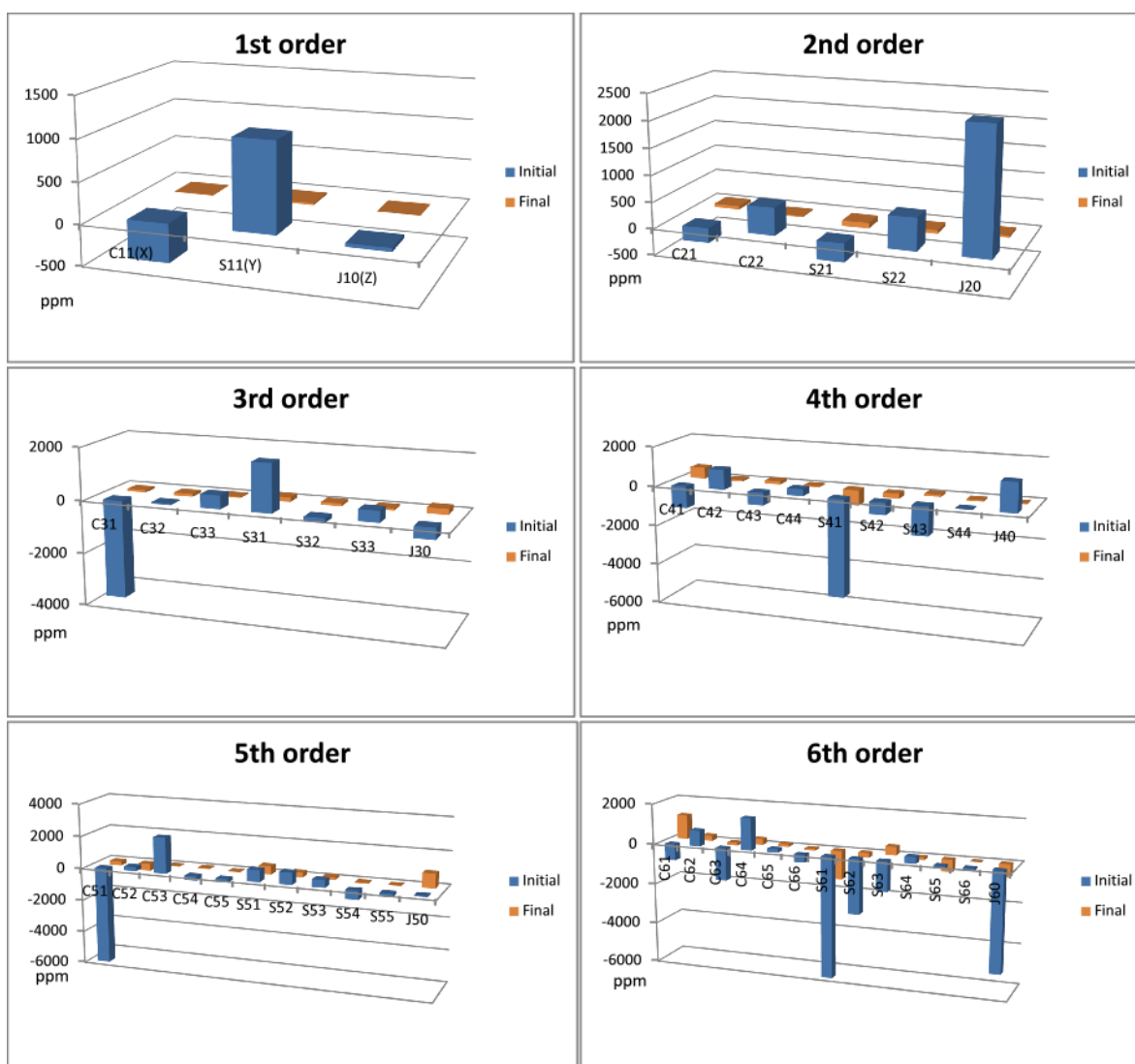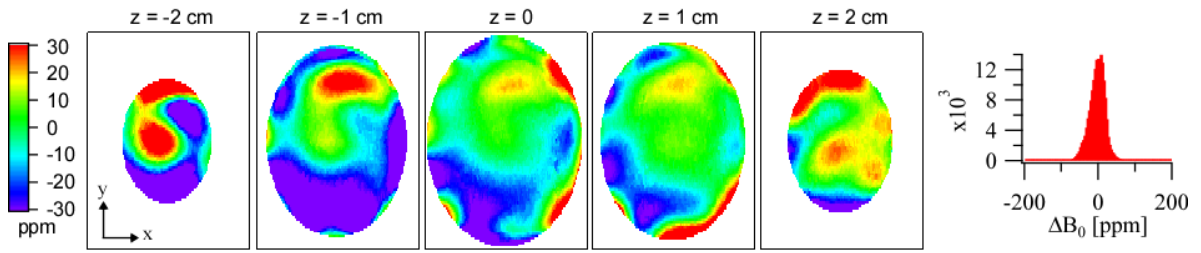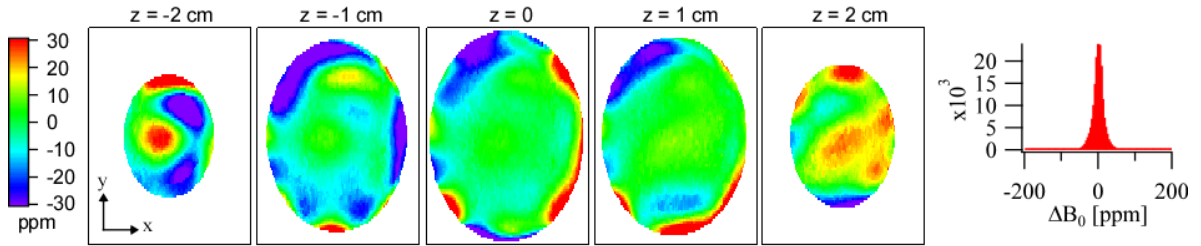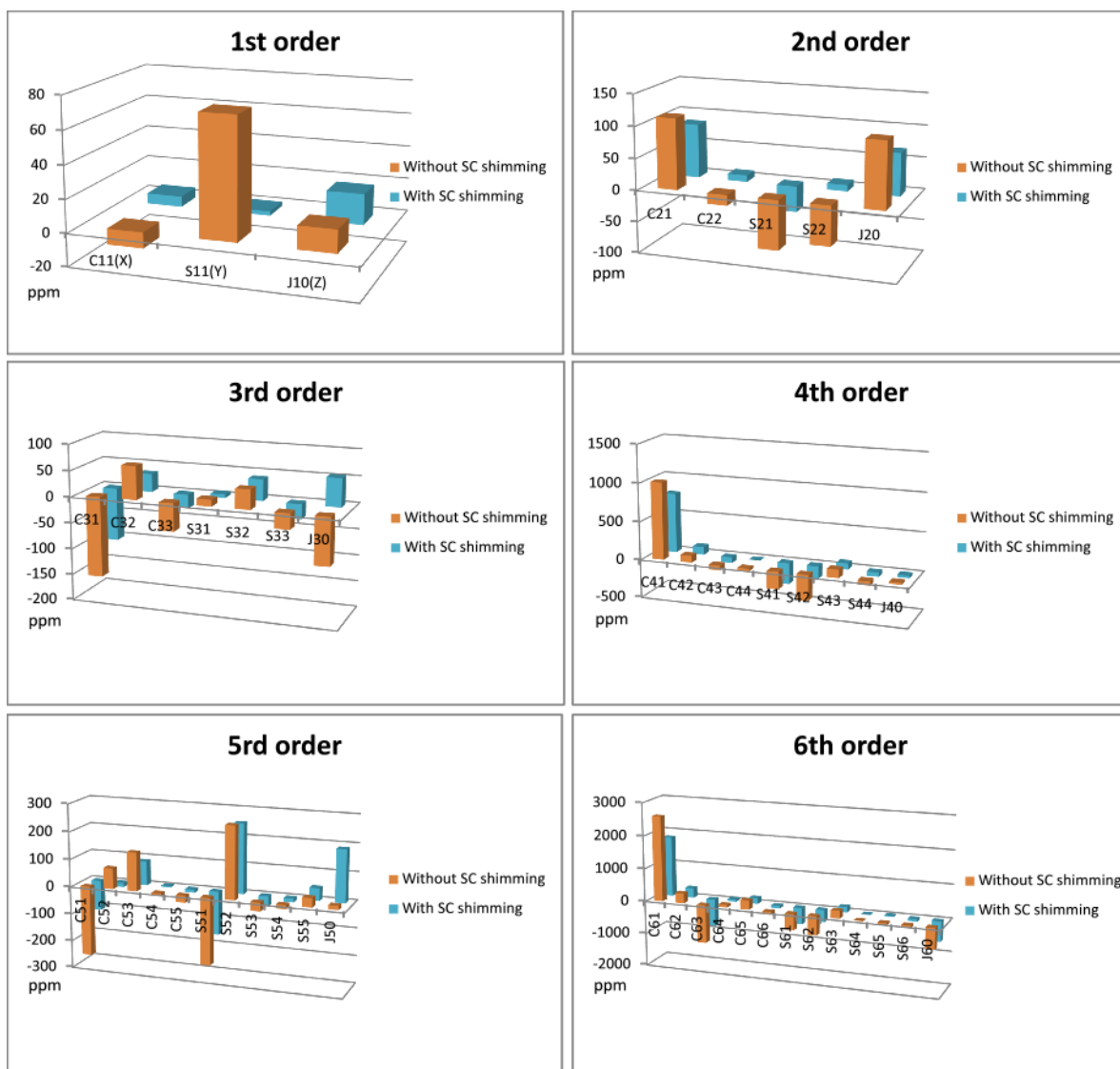
Fig. 5
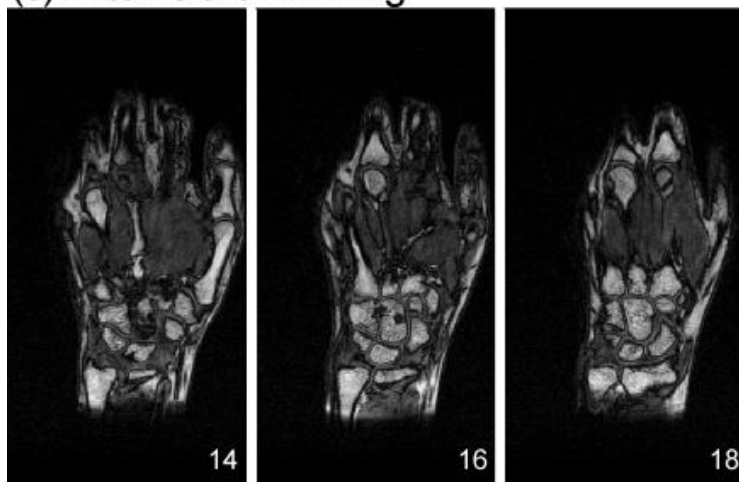
(a) Initial
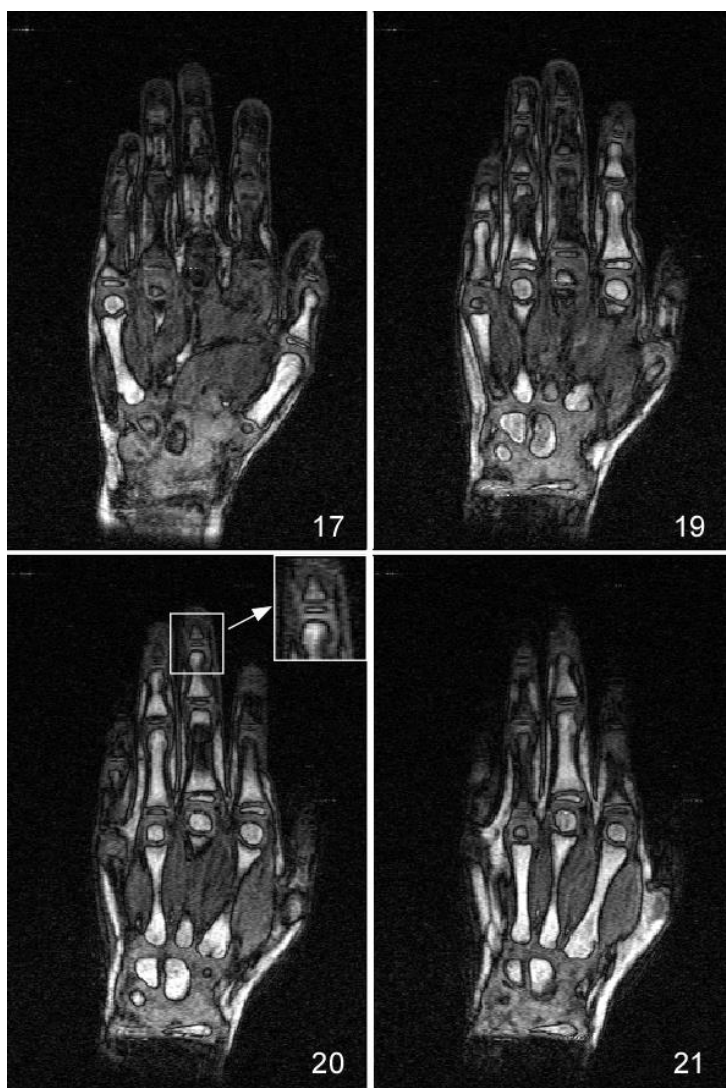
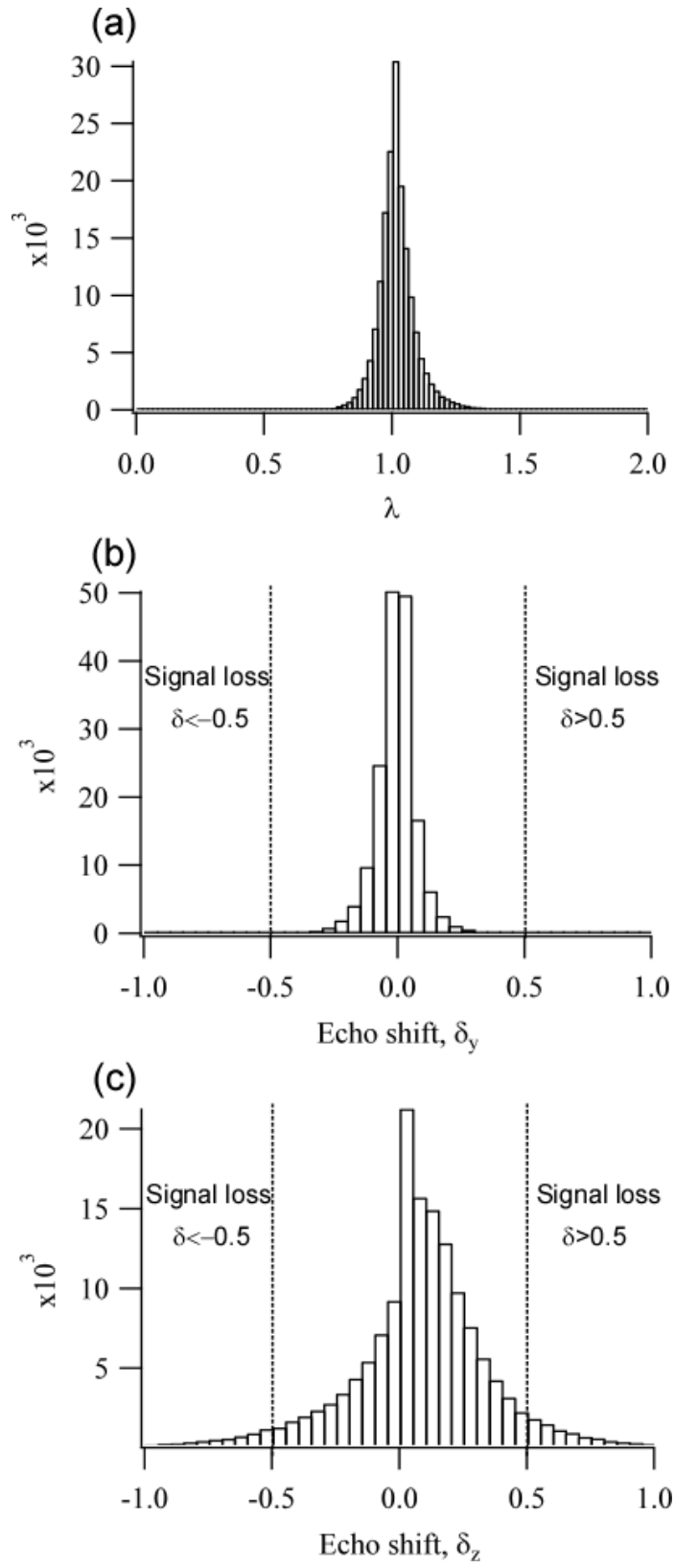(b) After passive shimming

(c) After SC shimming

Fig. 6

Fig. 7

Fig. 8